A multi-methodological study of kernite, a mineral commodity of boron

G. Diego Gatta[1], Alessandro Guastoni[2], Paolo Lotti[1], Giorgio Guastella[3],

Oscar Fabelo[4] and Maria Teresa Fernandez-Diaz[4]

[1]Dipartimento di Scienze della Terra, Università degli Studi di Milano,
Via Botticelli 23, I-20133 Milano, Italy
[2]Dipartmento di Geoscienze, Università degli Studi di Padova,
Via G. Gradenigo 6, I-35131, Padova, Italy
[3]Agenzia delle Dogane e dei Monopoli, Direzione Regionale per la Lombardia,
Ufficio Antifrode - Sezione Laboratorio, Via Marco Bruto 14, I-20138 Milan, Italy
[4]Institut Laue-Langevin, 71 Avenue des Martyrs, F-38000 Grenoble, France

Abstract

Kernite, ideally $Na_2B_4O_6(OH)_2 \cdot 3H_2O$, is one of the major constituent of the borate deposits and one of the most important mineral commodity of B. The chemical composition and the crystal structure of kernite from the Kramer Deposit (Kern County, California) were investigated by a series of analytical techniques (*i.e.*, titrimetric determination of B content, gravimetric method for Na, ion selective electrode for F, high-T mass loss for H_2O content, inductively coupled plasma atomic emission spectroscopy for REE and other minor elements, elemental analysis for C, N and H content) and by single-crystal X-ray (at 293 K) and neutron (at 20 K) diffraction. The concentration of more than 50 elements was measured. The general experimental formula of the kernite sample used in this study is: $Na_{1.99}B_{3.99}O_6(OH)_2 \cdot 3.01H_2O$. The fraction of other elements is, overall, insignificant: excluding B, kernite from the Kramer Deposit does not act as geochemical trap of other technologically-relevant elements (*e.g.*, Li, Be or REE). The X-ray and neutron structure model obtained in this study confirm that the structure of kernite is built up by: two (crystallographically independent) triangular BO_2OH groups and two tetrahedral BO_4 groups, which share corner-bridging O atoms to form 3-fold rings, giving chains running along [010], and $NaO_4(OH)(OH_2)$ and $NaO_2(OH)(OH_2)_3$ polyhedra. Positional disorder of two H sites of H_2O molecules was observed by the neutron structure refinement and corroborated by the maximum-entropy method calculation, which consistently provided a model based on a static disorder, rather than a dynamic one. The H-bonding network in the structure of kernite is complex, pervasive and play a primary role on its structural stability: the majority of the oxygen sites are involved in H-bonding, as *donors* or as *acceptors*. The potential utilizations of kernite, as source of B ($B_2O_3 \sim 50wt\%$), are discussed, on the basis of the experimental findings of this study.

76

77   **Keywords:** Kernite, borates, mineral commodity, X-ray diffraction, neutron diffraction, crystal

78   chemistry, hydrogen bonding.

79

80   **Introduction**

81   Kernite is a hydrous borate with ideal chemical formula $Na_2B_4O_6(OH)_2 \cdot 3H_2O$. It is a constituent

82   of sedimentary borate deposits, of which the more common minerals are borax (ideally

83    $Na_2[B_4O_5(OH)_4] \cdot 8H_2O$), ulexite (ideally $NaCa[B_5O_6(OH)_6] \cdot 5H_2O$), colemanite (ideally

84    $Ca[B_3O_4(OH)_3] \cdot H_2O$), kernite and tincalconite (ideally $Na_6[B_4O_5(OH)_4]_3 \cdot 8H_2O$). Ulexite, colemanite,

85   kernite, and tincalconite account for more than 90% of the borate minerals used by industry worldwide

86   (USGS 2019).

87   There is a raising interest to the light elements, in particular Li, B and Be, as technologically and

88   industrially relevant: they are currently considered as "critical elements" (or "critical raw materials",

89   according to the European Commission 2017), on the basis of their high economic importance and high

90   supply risk. Natural borates represent the most important source of boron. In 1998, the world production

91   on borates accounted for about 3.1 millions of tons; in 2009 the production increased to 4.5 Mtons and

92   in 2017 to 9.8 Mtons (USGS 2018, and previous reports). Only a few mineral commodities (and among

93   those Li) experienced such a trend of production and consumption over the last decades. The principal

94   reason of this raise is ascribed to the fact that boron is a strategic element for a series of technologically

95   relevant processes and products: *e.g.*, to produce heat-resistant glasses and ceramics, for the production

96   of boron-treated low-alloy steels (in which B is used to influence the hardenability and the behaviour of

97   the alloys at high temperature), for the production of radiation-shielding materials (due by the elevated

98   ability of ^{10}B to absorb thermal neutrons), as a critical micronutrient to the growth and health of plants

99   or as insecticide, as an effective photothermocatalyst for the conversion of carbon dioxide. Among the

100   aforementioned utilizations, one is referred to radiation emitted by nuclear reactors for energy

101   production, scientific research activities or medical applications (*i.e.*, boron neutron capture therapy -

102   BNCT), and it is the only one in which the isotopic signature of B plays an important role: ^{10}B shows a

103   high capacity to absorb thermal neutrons due to its high cross section for the $^{10}B(n,\alpha)^7Li$ reaction (~3840

104   barns; Carter et al. 1953, Sears 1986, Palmer and Swihart 1996, Rauch and Waschkowski 2002), whereas

105   that of ^{11}B is almost irrelevant (~0.006 barns). About 20% of natural boron occurs as ^{10}B.

106   In the framework of a long-term project to select potential B-bearing aggregates, we have recently

107   investigated the crystal chemistry and the stability at non-ambient conditions (at high and low

108   temperature, high pressure) of colemanite (Lotti et al. 2017, 2018, 2019) and kurnakovite (ideally

3

109 $Mg[B_3O_3(OH)_5]\cdot 5H_2O$, Gatta et al. 2019a) using a multi-methodological approach. We now extend our

110 crystal-chemical investigation to kernite, considering its availability in nature and the high B_2O_3 content

111 (~48wt%); this study will be followed by experiments on its *P-T* behaviour and chemical stability.

112   Only a few studies were so far dedicated to kernite. The first important description of this mineral is

113 ascribed to Schaller (1927), who provided optical parameters and a chemical wet analysis. Its crystal

114 structure was first reported by Amoros (1945) using X-ray diffraction techniques, and later reinvestigated

115 by Giese (1966), Cialdi et al. (1967), and Cooper et al. (1973). The X-ray structure refinement of Cooper

116 et al. (1973) is the last one reported in the open literature. Kernite crystallizes in the monoclinic *P*2$_1$/*c*

117 space group, with $a \cong 7.02$ Å, $b \cong 9.15$ Å, $c \cong 15.68$ Å, and $\beta \cong 108.9°$ (Z = 4). As observed in other

118 borates (*e.g.*, colemanite, kurnakovite), even kernite contains both triangular planar BO$_2$OH- and

119 tetrahedral BO$_4$-groups (Fig. 1). Two independent Na sites are sixfold-coordinated by O atoms, OH-

120 groups and H$_2$O molecules. One triangular BO$_2$OH group and two tetrahedral BO$_4$ groups share corner-

121 bridging O atoms to form 3-fold rings (3B:Δ + 2T or 3B:<Δ2[]>, according to the Heller 1996 and Grice

122 et al. 1999 notation), giving chains running along [010] and held together by hydrogen bonding (Fig. 1).

123 FT-IR and Raman spectra of kernite were reported and interpreted by Jun et al. (1995) and Kloprogge

124 and Frost (1999), and its high-pressure behaviour was later described by Silva et al. (2018) on the

125 basis of *in situ* IR and Raman spectra evolution collected in a diamond-anvil cell. Even the *T*-induced

126 dehydration behaviour (in vacuum and in air) of a natural kernite was reported by Sennova et al.

127 (2005), on the basis of thermo-gravimetric analysis and X-ray powder diffraction data. However, no

128 structural data (at room or at non-ambient conditions) are reported in the manuscripts of Jun et al.

129 (1995), Kloprogge and Frost (1999), Sennova et al. (2005) and Silva et al. (2018).

130   Despite the general structure model reported by Cooper et al. (1973) appears to be consistent (in terms

131 of bond distances and angles), their structure refinement provides only a partial view of the H-bonding

132 configuration, due to the limitation of the X-ray diffraction at that time. For example, some of the H sites

133 were described with isotropic displacement parameters up to six times larger (in Å^2) than others, which

134 could reflect a positional (static or dynamic) disorder. The occurrence of hydroxyl groups and cation-

135 coordinated H$_2$O, which account for a total H$_2$O content of about 26 wt%, generates the need for a

136 structure model with an accurate location of the H-sites. In addition, the very few chemical analyses of

137 kernite available in the open literature reported only the major constituents, and are based on analytical

138 protocols of the last century (Schaller 1927, Cipriani 1958, Hurlbut et al. 1973).

139   In this light, the aim of the present study is a reinvestigation of the crystal chemistry of kernite from

140 the Kramer Deposit (California), by single-crystal X-ray (at room conditions) and neutron diffraction

141 (at low temperature: 20 K) along with a series of other analytical techniques aimed to fully characterise

4

142 the chemical composition of the sample (*i.e.*, titrimetric determination of B content, gravimetric method

143 for Na, ion selective electrode for F, high-T mass loss for H_2O content, inductively coupled plasma

144 atomic emission spectroscopy - ICP-AES - for REE and other minor elements, elemental analysis for

145 C, N and H content). With this multi-methodological approach, we can provide: a description of the

146 chemical composition of kernite in terms of major and minor components, with a particular attention to

147 the potential B- and Na-substituents; an unambiguous location of all the proton sites and their vibrational

148 regime, along with a picture of the complex H-bonding network; a description of B-coordination

149 environment (*e.g.*, aplanarity of the triangular $BO_2(OH)$-group, polyhedral distortion of the tetrahedral

150 $BO_2(OH)_2$-groups).

151   The experimental findings of this study will be pivotal to fully understand if kernite can act as a carrier

152 of other technologically-relevant elements (*e.g.*, Li, Be, REE), its conditions of formation and

153 occurrence, its behaviour at non-ambient *P-T* conditions and the chemical reactivity, as its structure

154 stability appears to be substantially governed by the H-bonding network.

155

156   ## Sample description and occurrence

157   The sample of kernite used in this study belongs to the collection of the Museum of

158 Mineralogy of the University of Padova, Italy. The hand specimen is a colorless to white, glassy

159 fragment of a large centimetric crystal elongated parallel to the *c* axis and bounded by alternating

160 cleavage faces, nearly perfect, of the basal pinacoid *c* {001} and the prism *a* {100}.

161 The specimen was collected at the Kramer Deposit, Mohave desert, Kern County, California. Over

162 80 minerals were reported occurring in this deposit including a number of borates: borax, colemanite,

163 greigite, hydroboracite, inderite, inyoite, kernite, kurnakovite, meyerhofferite, probertite, searlesite,

164 tincalconite, tunellite and ulexite (Noble 1926, Schaller 1930, Morgan and Erd, 1969, Puffer 1975).

165 The Kramer deposit consists of a lenticular mass of kernite, borax and lower fraction of colemanite

166 and ulexite, measuring 1.6 km long, 0.8 km wide and up to 100 m thick. The borate minerals, several

167 hundred feet underground, occur in a complex clay series, underlain by igneous rock composed by

168 basaltic lavas, upper Miocenic in age and overlain by a stratigraphic series of continental arkosic

169 sands (Obert and Long 1962, Siefke 1991). For tens of meter deep, kernite is the only borate observed

170 in the deposit and it is the dominant mineral, so that the clay matrix is almost negligible in amount

171 (Schaller 1930). The mode of occurrence shows the deposit was originally composed only of borax

172 at the floor of a saline lake. Kernite increases abundance with depth, indicating that dehydration of

173 borax increases as a result of depth and pressure. Borax dehydration to kernite occurs under natural

174 conditions. When borax is exposed to open air, it alters to tincalconite, whilst kernite alteration to

5

175 tincalconite occurs only partially and very slowly. The abundance of kernite in the lower part of the

176 Kramer deposit suggests the temperature-pressure conditions from the borax-to-kernite reaction

177 occurs in the range 50-60 °C and about 750 meters deep (Christ and Garrels 1959).

178

179

180 **Experimental methods and Results**

181

182 **1) Titrimetric determination of the boron content**

183 A mass of 80-100 mg of kernite was placed in a 50 ml plastic test tube, along with 5 ml of

184 water and 3 ml of hydrochloric acid 1M. The plastic test tube was covered and transferred in an

185 ultrasound bath for 1-2 hours. The resulting clear solution was transferred in a 300 ml beaker, with

186 water up to about 100 ml of the total solution. A combined glass electrode (produced by InLab®

187 Routine Pro – Mettler Toledo) was immersed in the solution, and the pH was adjusted to 5.5-6.5 with

188 solutions of HCl 0.1-1M and NaOH 0.1-1M. A mass of 5-6 grams of mannitol was added and stirred,

189 until the complete dissolution of the solid phase. The solution was then titrated with NaOH 0.1M up

190 to pH 8.3-8.7. The content of acid titrated was completely due to the presence of boric acid in solution,

191 as the sample does not contain elements capable to hydrolyze the medium, or in general able to

192 influence its acidity. The measured fraction of B_2O_3 was 50.9(2) wt%.

193

194 **2) Gravimetric method to determine the sodium content**

195 A mass of 500-600 mg of kernite was placed in a weighed platinum crucible (m_1), acidified

196 with 20 ml of hydrochloric acid 1:1 and evaporated to dryness. Residue was treated with 25 ml of

197 methyl alcohol and 10 ml of concentrated hydrochloric acid, and evaporated to dryness. The latter

198 operation was repeated 4-5 times. Residue, in absence of other elements at a significant level (see

199 other analyses) is pure NaCl. Platinum crucible was dried in an oven at 110-130°C for 1-2 h, cooled

200 in a desiccator and weighed (m_2). The different of weigh ($m_2 - m_1$) is the Na content in the mineral,

201 expressed as NaCl. The measured fraction of Na_2O was 22.6(2) wt%.

202

203 **3) Determination of fluorine content**

204 A mineral sample of 20 mg in mass was placed in a 50 ml plastic test tube, along with 5 ml of

205 water and 3 ml of hydrochloric acid 1M. The plastic test tube was covered and transferred in an

206 ultrasound bath for 1-2 hours. A volume of 2-3 ml of Total Ionic Strength Adjustment Buffer

207 (Commercial solution TISAB III) was added to the clear solution and diluted to 20 ml with water.

6

208   The F content ~~then~~ was then determined using the perfectION™ Combination Fluoride Ion Selective

209   Electrode (Mettler Toledo), adopting the conventional method of standard addition. Solutions of

210   fluorine from 0.1 to 5.0 mg/l were prepared by Certified Reference Material - CRM 1000 mg/l of

211   fluorine. The resulting F fraction was 0.01 wt% (uncertainty not determined).

212

213   **4) Determination of H_2O content by heating**

214   A mass of 500-600 mg of sample was placed in a quartz crucible with lid, and gradually heated

215   in a muffle furnace from 20°C up to 800°C. Assuming that the mass loss represents the total amount

216   of H_2O, the estimated H_2O fraction of the kernite sample was 26.4(2) wt%.

217

218   **5) Determination of minor elements by inductively coupled plasma atomic emission**

219   **spectroscopy (ICP-AES)**

220   All determinations were performed in axial view mode for REE, and radial view mode for the

221   other minor elements, with a Perkin Elmer Optima 7000DV ICP-AES spectrometer.

222

223   *5.1)   Determination of REE concentration by ICP-AES*

224   A mass of 50 mg of kernite sample was placed in a 50 ml plastic test tube, along with 5 ml of

225   water and 3 ml of hydrochloric acid 1M. The plastic test tube was covered and transferred in an

226   ultrasound bath for 1-2 hours. The resulting clear solution was then transferred in a 50 ml volumetric

227   flask and diluted with water. A calibration protocol was performed with a blank solution and a series

228   of solutions prepared with: similar fractions of sodium and boron as those of the sample under

229   investigation and REE concentration from 0.001 to 0.050 mg/l for each element (using CRM multi

230   elemental standard mix for ICP). Results and instrumental parameters are listed in Table 1.

231

232   *5.2)   Determination of other minor elements concentration by ICP-AES*

233   The determination of the non-REE minor elements was performed using two different

234   protocols, described below:

235   i)   A mass of 10-20 mg of kernite sample was placed in a 50 ml plastic test tube, along

236   with 5 ml of water and 3 ml of hydrochloric acid 1M. The plastic test tube was covered

237   and transferred in an ultrasound bath for 1-2 hours. The resulting clear solution was

238   then transferred and diluted with water in a 25 ml volumetric flask, containing 2.5 ml

239   of scandium solution (100 mg/l) as internal standard. A calibration protocol was

240   adopted with a blank solution and a series of 5 solutions prepared with concentration

7

241   between 0.05 and 1.0 mg/l for each element (using CRM multi elemental standard mix

242   for ICP).

243   ii)   Decomposition by alkaline fusion of 10-20 mg of kernite sample in platinum crucible

244   with 100 mg of sodium or potassium carbonate in a muffle furnace at 1000°C for 5

245   minutes, followed by dissolution in 10 ml of water and 1 ml of sulphuric acid 1M or 1

246   ml of hydrochloric acid 1M. The clear solution was then transferred and diluted with

247   water in a 25 ml volumetric flask containing 2.5 ml of scandium solution (100 mg/l)

248   as internal standard. A calibration protocol was adopted with a blank solution and a

249   series of 5 solutions prepared with concentration ranging between 0.05 amd 1.0 mg/l

250   for each element (using CRM multi elemental standard mix for ICP).

251   Results and instrumental parameters are given in Table 2.

252

253

6) Determination of C, N, and H

255   200-300 mg of mineral sample were decomposed at 950°C in an elementary analyzer LECO

256 Truspec CHN, in excess of oxygen for 90 seconds. The decomposition products were transferred to

257 a second furnace (Afterburner) at 850°C for a further oxidation and particulate removal. After

258 collection and homogenization of the gases in a container of 4.5 liters at 50°C, Infrared absorption

259 detectors were used to measure the CO_2 and H_2O concentration (as the C concentration was measured

260 in the form of CO_2 and the H one in the form of H_2O). A different portion of the decomposition

261 products was instead transferred in a stream of helium through a copper catalyst in order to convert

262 NO_X to N_2 and to remove oxygen, carbon dioxide and water. A thermal conductivity detector was

263 used to determine the N_2 content. EDTA, sodium tetra-borate deca-hydrate, boric acid, calcium

264 carbonate, sodium nitrate and acid oxalic di-hydrate were employed as calibration standards. The

265 measured fractions were: C < 0.02 wt% (uncertainty not determined), N < 0.02 wt% (uncertainty not

266 determined), and H = 3.0(2) wt%.

267

268 A representative chemical composition of kernite from the Kramer deposit is given in Table 3, and

269 its experimental chemical formula is virtually identical to the ideal one: $Na_2B_4O_6(OH)_2 \cdot 3H_2O$.

270

271

8

7) Single-crystal X-ray and neutron diffraction

7.1) *X-ray and neutron data collections and treatments*

Single-crystal X-ray diffraction data were collected, at room temperature, with a Rigaku XtaLABSynergy-i diffractometer, equipped with a PhotonJet-i Mo$K\alpha$ microfocus source and a HyPix-6000HE Hybrid Photon Counting (HPC) detector, at the Earth Science Dept. Univ. Milan. To maximize the reciprocal space coverage and the quality of the intensity data, a series of collection runs were optimised using the *ad hoc* routine of the CrysAlisPro™ suite (Rigaku – Oxford Diffraction 2019), with ω scan strategy, step size of 0.5° and an exposure time per frame of 2 s. A total number of 13010 reflections up to $2\theta_{max}$ of 60° was collected (with $-9 \le h \le +8$, $-12 \le k \le +12$ and $-19 \le l \le +20$), out of which 2296 were unique ($R_{int} = 0.0361$, Laue class $2/m$) and 1908 with $F_o > 4\sigma(F_o)$, giving a metrically monoclinic unit-cell with: $a = 6.9983(3)$, $b = 9.1375(3)$, $c = 15.6389(7)$ Å, $\beta = 108.832(5)°$ and $V = 946.53(7)$ Å^3 (Table 4). Corrections for Lorentz-polarization effects and (semi-empirical) X-ray absorption were applied using the *ABSPACK* routine, implemented in the CrysAlisPro™ package (Rigaku – Oxford Diffraction 2019). The systematic extinctions were consistent with the space group $P2_1/c$. X-ray intensity data were then processed with the *E-STATISTICS* program, implemented in the *WinGX* package (Farrugia 1999): the statistics of distributions of the normalized structure factors showed that the structure is centrosymmetric at ∼93% likelihood (the Sheldrick's $\lvert E^2\text{-}1 \rvert$ criterion is 0.969).

Single-crystal neutron diffraction data were collected at low temperature from a crystal of kernite (approx. 3 x 2 x 2 mm^3) on the four-circle diffractometer D9 at the Institut Laue-Langevin (ILL), Grenoble (Gatta et al. 2019b). The crystal was glued on a vanadium pin and placed on a close-circuit displex device operated at 20.0(5) K (Archer and Lehmann 1986). The wavelength of 0.8347 Å, obtained from a Cu(220) monochromator, and a small two-dimensional area detector were used. The measurement strategy consisted of a series of ω-scans or ω-2θ scans for low and high-Q reflections, respectively. The Bragg reflections were collected varying the ω-range as a function of the instrument resolution curve. A total number of 3434 reflections were collected (with $-10 \le h \le +10$, $0 \le k \le +18$ and $-23 \le l \le +24$), out of which 3161 were unique ($R_{int} = 0.0488$, Laue class $2/m$) and 2656 with $F_o > 4\sigma(F_o)$, with $d_{min} = 0.59$ Å (Table 4). Intensity integration, background and Lorentz factor correction of the scans were done with the Racer program (written by Clive Wilkinson and Garry McIntyre, ILL integration program suite, https://forge.ill.fr/projects/sxtalsoft/repository/show/racer). The lattice was found to be metrically monoclinic (Table 4), and consistent with the X-ray experimental findings reported above. Absorption correction was applied, based on composition and shape of the crystal using the ILL

9

305   program Datap (the current version of this program is available online on https://forge.ill.fr/). The

306   reflection conditions were found to be consistent with the space group $P2_1/c$. The Wilson plot and the

307   statistics of distributions of the normalized structure factors showed that the structure is

308   centrosymmetric at ~91% likelihood (the Sheldrick's $\left| E^2\text{-}1 \right|$ criterion is 0.958).

309   Further details pertaining to the X-ray and neutron data collection strategies are listed in Table

310   4 (*deposited*).

311

312   ### 7.2) *X-ray and neutron structure refinements*

313   Anisotropic crystal-structure refinements, based on the X-ray and neutron intensity data,

314   collected at room and at low *T,* respectively, were conducted in the space group $P2_1/c$ using the

315   SHELXL-97 software (Sheldrick 1997, 2008), and starting from the structure model of Cooper et al.

316   (1973), without any H atom. Neutral X-ray scattering factors of Na, B, O and H were taken from the

317   *International Tables for X-ray Crystallography (Vol. C)* and used for the X-ray refinement, whereas

318   neutron scattering lengths of Na, B, O and H were taken from Sears (1986). Secondary isotropic

319   extinction effect was corrected according to the formalism of Larson (1967).

320   For both the refinements (*i.e.*, X-ray at 293 K and neutron at 20 K), convergence was rapidly

321   achieved after the first cycles, with a series of residual peaks in the final difference-Fourier map of

322   the electron or nuclear density (positive for the X-ray refinement, negative for the neutron

323   refinement). The complex configuration of the H population was first modelled on the basis of the

324   neutron data, and then implemented in the X-ray refinement. The negative residual peaks found in

325   the difference-Fourier map of the nuclear density were assigned to the H sites in the next cycles (*i.e,*

326   H has a negative neutron scattering length). Shape and magnitude of the minima in the difference-

327   Fourier maps showed no evidence of positional or dynamic disorder for six of the H sites (*i.e.*, H1-

328   H6, Table 5). However, evidence of disorder was observed for the H population bonded to the

329   (opposite) O8 and O11 sites, which are vertices of the Na1 and Na2 polyhedra, respectively (Fig. 2,

330   Table 5). After a series of tests, the best figures of merit was obtained with three H sites bonded to

331   O8 [*i.e.*, H6, H72 and H82, with site occupancy factor *s.o.f.*(H2) = 1 and *s.o.f.*(H72)+*s.o.f.*(H82) = 1]

332   and three bonded to O11 [*i.e.*, H1, H71 and H81, with *s.o.f.*(H1) = 1 and *s.o.f.*(H71)+*s.o.f.*(H81) = 1],

333   with the following mutually exclusive configurations: (H6-O8-H82 + H1-O11-H71) and (H6-O8-

334   H72 + H1-O11-H81) (Fig. 2, Table 5). With such a structure model, convergence was achieved and

335   the variance-covariance matrix showed no significant correlation among the refined variables; all the

336   principal mean-square atomic displacement yent parameters were positive (including those for the H sites,

337   Table 6) and the final $R_1(F) = 0.0723$, for 2656obs./226par. (Table 4 - *deposited*).

10

338   Implementing the structure model based on the neutron refinement, even convergence of the

339   X-ray refinement was rapidly achieved, with no significant correlation among the refined variables.

340   The final $R_1(F) = 0.0324$, for 1908obs./193par. (Table 4 - *deposited*).

341   Additional details pertaining to structure refinements are given in Table 4 (*deposited*). Atomic

342   coordinates and displacement parameters are listed in Tables 5 (*deposited*) and 6 (*deposited*); selected

343   interatomic distances and angles are given in Table 7.

344   In order to corroborate (or deny) the structure model based on the neutron least-square

345   refinement, with its disordered H-sites configuration, nuclear density distribution was also analysed

346   by the maximum-entropy method (MEM), using the program DYSNOMIA (Momma et al. 2013) and

347   the graphical representation of nuclear density maps by VESTA (Momma and Izumi 2011). The

348   nuclear density maps were obtained from the single-crystal neutron data collected at 20 K. 2435

349   unique reflections with $I/\sigma(I) > 3$ where used in the MEM calculation giving rise a final $R(F)$ and

350      $wR(F)$ of 3.7 and 3.5 %, respectively. A grid of 256 x 256 x 256 voxels were used to obtain a detailed

351   density map. Fig. 3 shows a section of the nuclear density function corresponding to the (0.1, 0.5,

352   0.6) plane. This plane was selected as O8, O11 and symmetry-related H_2O molecules lay on it.

353

354   **Discussion and Implications**

355   Chemical and structural analysis of the kernite sample under investigation confirm the general

356   formula previously reported in the literature: $Na_2B_4O_6(OH)_2 \cdot 3H_2O$. The only potential substituents of

357   Na^+ here detected, distributed in the two independent Na1 and Na2 sites and giving distorted

358   coordination polyhedra with CN = 6, are represented by Mg^{2+} and K^+, but their sum is less than 0.01

359   *a.p.f.u.* (Table 3). Similarly, the only potential substituents of B^{3+} (in tetrahedral coordination) are

360   Si^{4+} and Al^{3+}, but for less than 0.01 *a.p.f.u.* (Tables 2 and 3). Even the F^- fraction, as potential OH-

361   group substituent, is not significant (*i.e.*, < 0.01 *a.p.f.u.*, Tables 2 and 3). The concentration of other

362   minor elements and of the REE is substantially irrelevant, as shown in Tables 1 and 2. Overall, kernite

363   does not show any significant isomorphic substitution, and thus cannot act as geochemical trap of

364   technologically-relevant elements (*e.g.*, Li or REE). This finding can be compared with the results

365   that we recently obtained on other borates: even in colemanite ($Ca[B_3O_4(OH)_3] \cdot H_2O$, from the Bigadiç

366   Mine, Balikesir Province, Marmara Region, Turkey; Lotti et al. 2018, 2019) and in kurnakovite

367   ($Mg[B_3O_3(OH)_5] \cdot 5H_2O$, from the Kramer Deposit, Mohave desert, Kern County, California; Gatta et

368   al. 2019a) no significant isomorphic substituents were found, so that the experimental formulae were

369   virtually identical to the ideal ones. In this light, the surprising chemical purity observed for kernite

370   in this study, and previously in colemanite and kurnakovite (for which a similar chemical analytical

11

371   protocol was used; Gatta et al. 2019a; Lotti et al. 2018, 2019), appears not to be a peculiarity of the

372   single species or of a given deposit, but it is rather a common feature of the hydrous borates which

373   share the same geological environment: lacustrine deposits with hydrothermal activity. The reasons

374   for such a high purity are still obscure: whereas it is more difficult to find a substituent of B (in CN 3

375   or 4), which generates a low chemical strain into the structure, Na could be efficiently replaced by

376   alkaline or even earth-alkaline cations, if we consider the bonding configuration of the (distorted) Na-

377   polyhedra in the kernite structure (Table 7). The same considerations, though referred to different

378   cations, were previously done on colemanite and kurnakovite by Gatta et al. (2019a). However, the

379   chemical composition of a given hydrothermal mineral it is not only dictated by its crystal structure,

380   but even by the composition of the solution. In this light, a possible explanation is that crystal

381   nucleation and growth could promote purification by iterated dissolution and recrystallization.

382   The structure model of kernite obtained in this study, based on X-ray and neutron diffraction

383   data, is (partially) consistent with that previously reported by Cooper et al. (1973). The structure is

384   built by two crystallographically independent triangular BO_2OH groups (with the B-ions in sp^2

385   electronic configuration) and two tetrahedral BO_4 groups (with the B-ions in sp^3 electronic

386   configuration), which share corner-bridging O atoms to form 3-fold rings (3B:Δ + 2T units), giving

387   chains running along [010] and held together by hydrogen bonding (Fig. 1). Two independent Na sites

388   are sixfold-coordinated by O atoms, OH-groups and H_2O molecules, though the bonding configuration

389   of the strongly distorted Na2-polyhedron would suggest a CN = 5+1, as five Na2-O distances are shorter

390   than 2.5 Å and one is about 3.1 Å (Table 7, room-T X-ray refinement).

391   The X-ray (data collected at 293 K) and neutron (data collected at 20 K) structure refinements

392   consistently show that:

393   1) The triangular [$BO_2(OH)$]-groups have an almost ideal configuration, with Δ(B1-O)$_{max}$ ~

394   Δ(B4-O)$_{max}$ ~ 0.02-0.03 Å (*i.e.*, the difference between the longest and the shortest bond

395   distances), average O-B-O angles of 120° (ranging between 118.5°-122.8° for B1- and

396   115.3°-124.4° for B4-triangular groups), and aplanarity < 1° (here defined as the average

397   angle described by the plane on which the 3-oxygen sites lie and each of the three

398   independent B-O$_n$ vectors); the tetrahedral [BO_4]-groups are only slightly distorted, with

399   Δ(B2-O)$_{max}$ ~ Δ(B3-O)$_{max}$ ~ 0.06 Å; the Na1O$_4$(OH)(OH$_2$) polyhedron has Δ(Na1-O)$_{max}$ ~

400   0.22 Å and is less distorted than the Na2O$_2$(OH)(OH$_2$)$_3$ one with Δ(Na2-O)$_{max}$ ~ 0.7 Å. The

401   B-O and Na-O distances are slightly different as a function of bonding configuration of the

402   oxygen sites (*i.e.*, oxygen of a OH- or OH$_2$-group or as a bridging site between polyhedra).

12

2) Three crystallographically independent H_2O molecules occur in the structure of kernite (*i.e.*, H3-O10-H5, H6-O8-H72 or H6-O8-H82, H1-O11-H71 or H1-O11-H81, Table 7). Among those, two are affected by positional disorder of the H sites, so that two mutually exclusive configurations occur, here modelled as: (H6-O8-H82 + H1-O11-H71) or (H6-O8-H72 + H1-O11-H81) (Figs. 2 and 4). The results obtained by the structure refinements are consistent with a model based on a static disorder of the H sites, rather than a dynamic one. The nuclear density distribution around pairs of the oxygen atoms O8 and O11 obtained by MEM confirm a double well potential, which gives rise to a splitting of the H sites (Fig. 3). The nuclear density maps indicate that the H71/H72 and H81/H82, and those related by symmetry, could be modelled using a statically disordered configuration with hydrogen atoms filling two well defined sites. The unbalanced nuclear density between each hydrogen position suggests a non-equivalent occupancy of each site, in agreement with the refined structural model (Table 5). However, other scenarios could also explain the observed H network. Two different hydrogen networks are derived from the current model, one configuration if H71 and H82 are present and a second for the case of H72 and H81. The H71 and H72 sites could be seen as a splitting of the hydrogen atom located between two opposite oxygen sites (in this case: O8 and O11). A similar scenario was reported for ice phases, where the jump between both configurations was ascribed to "proton tunnelling" (Bove et al. 2009, Yen and Gao 2015). The tunnelling occurs at low temperature when a proton has the same probability to be located on each minimum of a double well potential. Therefore, this effect involves, in most of the cases, symmetric potentials. In our case, the nuclear density maps obtained from the MEM clearly show that both sites have not the same density, and therefore a different energy barrier occurs in each well of potential. Although a proton tunnelling could not completely discarded, based on the current results this scenario is unlikely.

It is worth noting that a similar kind of disorder of the H_2O hydrogen atoms also occurs in colemanite (Lotti et al. 2018), leading to two possible (and mutually exclusive) H-bonding configurations.

3) Geometrically, the three crystallographically independent H_2O molecules show: *a*) H-O-H angles ranging between 102° and 108° (neutron data), consistent with the observed H-O-H angles in solid-state materials (*e.g.*, Steiner 1998, and references therein; Gatta et al. 2008, 2012, 2019a; Lotti et al. 2018); *b*) O-H distances (corrected for "riding motion effect" following Busing and Levy 1964) ranging between 0.98 and 1.05 Å (neutron data); *c*) O–

13

436   H…O angles $\geq$ 162° (Table 7), approaching a configuration energetically favourable (*i.e.*,

437   toward linearity), and O$_{donor}$…O$_{acceptor}$ distances of about 2.7-2.8 Å (Table 7, neutron data).

438   The two independent hydroxyl groups (*i.e.*, O6-H2 and O7-H4, Table 7) show O-H

439   distances (corrected for "riding motion effect") ranging between 0.98-0.99 Å,

440   O$_{donor}$…O$_{acceptor}$ distances between 2.8-3.3 Å, and O-H...O >172° (Table 7, neutron data).

441   4) If we exclude O4 and O9, all the other oxygen sites in the structure of kernite are involved

442   in H-bonding, as *donors* or as *acceptors* (Fig. 4, Table 7).

443   5) The X-ray and neutron refinements, based on the intensity data collected at 293 and 20 K

444   respectively, show that this borate does not experience any *T*-induced phase transition,

445   within the *T*-range investigated. The two structure models are virtually identical. As

446   expected, there is a drastic reduction of the magnitude of the atomic displacement ellipsoids

447   at low *T*, as shown by the U_{eq} values (calculated as one third of the trace of the

448   orthogonalised U_{ij} tensor, Tables 5 and 6 - *deposited*). Some of the atomic displacement

449   ellipsoids are significantly anisotropic at 20 K (Table 6 - *deposited*, Figs. 1, 2 and 4), though

450   still realistic. We are inclined to believe that this is the twofold effect generated by: *a*) a not

451   efficient correction for the extinction effect with the isotropic model of Larson (1967) and

452   *b*) the static disorder of the H-sites belonging the H$_2$O molecules of the Na1- and Na2-

453   polyhedra, which affect all the sites of the Na-coordination shells.

454 The structure model obtained in this study is consistent with the FT-IR and Raman spectra of kernite

455 reported and interpreted by Jun et al. (1995), Kloprogge and Frost (1999) and Silva et al. (2018). The

456 experimental findings of this study confirm that also in kernite, as for other hydrous borates (Gatta et

457 al. 2019a), the H-bonding network is complex, pervasive and play a primary role into the crystalline

458 edifice. This could also explain the almost insignificant F$^-$ (or even Cl$^-$) *vs.* OH$^-$ substitution (Table

459 3). The first implication on potential utilizations of kernite is that any environmental variable able to

460 affect the H-bonding network (*i.e.*, under chemical, thermal or compressional stress conditions) can

461 generate a structure instability. This can be deduced, for example, by the thermal behaviour of kernite

462 reported by Sennova et al. (2005; without structure refinement) or by the static compressional

463 behaviour reported by Silva et al. (2018; without structure refinement), along with the reported

464 solubility in water (Mineral Data Publishing, http://rruff.info/doclib/hom/kernite.pdf). However, the

465 mechanisms, at the atomic scale, that govern the thermal and compressional behaviour of kernite are

466 still obscure, and will be the aim of our future experiments, based on *in situ* X-ray diffraction

467 investigations.

14

468   The solubility of kernite in water (or in other polar solvents) could be considered a positive feature

469   for a mineral commodity of B, which contains up to 15 wt% of elemental B (B_2O_3~50 wt%). However,

470   the potential utilization of kernite as B-rich aggregate in Portland cement concretes (used as radiation-

471   shielding materials for the elevated ability of ^{10}B to absorb thermal neutrons) is hindered by its high

472   Na content (16 wt% of elemental Na; Na_2O 21.3 wt%), which could promote deleterious reactions

473   for the durability of cements (*e.g.*, the so-called "alkali-silica reactions" – ASR). The national

474   standards are not identical in the different countries but, in general, the alkali content in ordinary

475   Portland cements (calculated by $Na_2O + 0.658 \cdot K_2O$, the so-called "$Na_2O_{equivalent}$") should not exceed

476   0.60 wt%, in order to avoid or minimize the risk of ASR. However, it is still obscure the role of Na

477   and B in Sorel cements (*i.e.*, magnesium oxychloride cements), leaving room for experiments in this

478   direction. Sorel cements are not used as reinforced concretes, as basically incompatible with steel

479   reinforcement because the presence of chloride, but are commonly used to make floor tiles and panels

480   for fire protection. Could B-additivated Sorel cements be efficiently used for the production of

481   radiation-shielding tiles or panels?

482

483

492

493

494

References

495   Amoros, J.L.P. (1945) La estructura de la kernita. Euclides, 57-58, 599-608.

497   Archer, J. and Lehmann, M.S. (1986) A simple adjustable mount for a two-stage
498   cryorefrigerator on an Eulerian cradle. Journal of Applied Crystallography, 19, 456-459.

499   Bove, L.E., Klotz, S., Paciaroni, A., and Sacchetti, F. (2009) Anomalous Proton Dynamics in
500   Ice at Low Temperatures. Physical Review Letter, 103, 165901-4.

501   Busing, W.R. and Levy, H.A. (1964) The effect of thermal motion on the estimation of bond
502   lengths from diffraction measurements. Acta Crystallographica, 17, 142-146.

503   Carter, R.S., Palevsky, H., Myers, V.W., and Hughes, D.J. (1953) Thermal neutron absorption
504   cross sections of boron and gold. Physical Review, 96, 716-721.

505   Christ, C.L. and Garrels, R.M. (1959) Relations among sodium borate hydrates at the Kramer
506   deposit, Born, California. American Journal of Science, 257, 516-528.

507   Cialdi, G., Corazza, E., and Sabelli, C. (1967) La struttura cristallina della kernite,
508    $Na_2B_4O_6(OH)_2 \cdot 3H_2O$. Rendiconti dell'Accademia Nazionale dei Lincei, Ser. VIII, 42, 236-251.

509   Cipriani, C. (1958) Ricerche sulla disidratazione di alcuni borati naturali. Atti della Società
510   Toscana di Scienze Naturali, 65A, 284-322.

511   Cooper, W.F., Larsen, F.K., and Coppens, P. (1973) Electron population analysis of accurate
512   diffraction data. V. Structure and one-center charge refinement of the light-atom mineral kernite,
513    $Na_2B_4O_6(OH)_2 \bullet 3H_2O$. American Mineralogist, 58, 21-31.

514   European Commission (2017) Critical Raw Materials for the EU. Document 52017DC0490,
515   https://ec.europa.eu/growth/sectors/raw-materials/specific-interest/critical_en.

516   Farrugia, L.J. (1999) WinGX suite for small-molecule single-crystal crystallography. Journal
517   of Applied Crystallography, 32, 837-838.

518   Gatta, G.D., Rotiroti, N., McIntyre, G.J., Guastoni, A., and Nestola, F. (2008) New insights
519   into the crystal chemistry of epididymite and eudidymite from Malosa, Malawi: a single-crystal
520   neutron diffraction study. American Mineralogist, 93, 1158-1165.

521   Gatta, G.D., McIntyre, G.J., Swanson, G.J., and Jacobsen, S.D. (2012) Minerals in cement
522   chemistry: a single-crystal neutron diffraction and Raman spectroscopic study of thaumasite,
523    $Ca_3Si(OH)_6(CO_3)(SO_4) \cdot 12H_2O$. American Mineralogist, l97, 1060-1069.

524   Gatta G.D., Guastoni A., Lotti P., Guastella G., Fabelo O., Fernandez-Diaz. M.T. (2019) A
525   multi-methodological study of kurnakovite: A potential B-rich aggregate. American Mineralogist,
526   104, 1315-1322.

16

527   Gatta, G.D., Fabelo-Rosa O.R., and Fernandez-Diaz M.T. (2019b) Crystal chemistry of kernite

528   mineral [$Na_2B_4O_6(OH)_2 \cdot 3H_2O$]: a sustainable approach for boron-based cements. Experimental

529   Report, Institut Laue-Langevin (ILL), doi:10.5291/ILL-DATA.DIR-179.

530   Giese, R. F. Jn. (1966) Crystal structure of kernite, $Na_2B_4O_6(OH)_2 \cdot 3H_2O$. Science, 154, 1453-

531   1454.

532   Grice, J.D., Burns, P.C., and Hawthorne, F.C. (1999) Borate minerals. II. A hierarchy of

533   structures based upon the borate fundamental building block. Canadian Mineralogist, 37, 731-762.

534   Heller, G. (1986) A survey of structural types of borates and polyborates. Topics in Current

535   Chemistry, 131, 39-98.

536   Hurlbut, C. S. Jr., Aristarain, L.F., and Erd, R.C. (1973) Kernite from Tincalayu, Salta,

537   Argentina. American Mineralogist, 58, 308-313.

538   Jun, L., Shuping, X., and Shiyang, G. (1995) FT-IR and Raman spectroscopic study of hydrated

539   borates. Spectrochimica Acta Part A: Molecular and Biomolecular Spectroscopy, 51, 519-532.

540   Kloprogge, J.T. and Frost, R.L. (1999) Raman microscopic study of some borate minerals:

541   Ulexite, kernite, and inderite. Applied spectroscopy, 53, 356–364.

542   Larson, A.C. (1967) Inclusion of secondary extinction in least-squares calculations. Acta

543   Crystallographica, 23, 664-665.

544   Lotti, P., Gatta, G.D., Comboni, D., Guastella, G., Merlini, M., Guastoni, A., and Liermann, H.P.

545   (2017) High-pressure behavior and P-induced phase transition of $CaB_3O_4(OH)_3 \cdot H_2O$ (colemanite).

546   Journal of American Ceramic Society, 100, 2209-2220.

547   Lotti, P., Gatta, G.D., Demitri, N., Guastella, G., Rizzato, S., Ortenzi, M.A., Magrini, F.,

548   Comboni, D., Guastoni, A., and Fernandez-Diaz, M.T. (2018) Crystal-chemistry and temperature

549   behavior of the natural hydrous borate colemanite, a mineral commodity of boron. Physics and

550   Chemistry of Minerals, 45, 405-422.

551   Lotti, P., Comboni, D., Gigli, L., Carlucci, L., Mossini, E., Macerata, E., Mariani, M., and Gatta,

552   G.D. (2019) Thermal stability and high-temperature behavior of the natural borate colemanite: An

553   aggregate in radiation-shielding concretes. Construction and Building Materials, 203, 679–686.

554   Momma, K., and Izumi, F. (2011) Vesta 3 for three-dimensional visualization of crystal,

555   volumetric and morphology data. Journal of Applied Crystallography, 44, 1272-1276.

556   Momma, K., Ikeda, T., Belik, A.A., and Izumi, F. (2013) Dysnomia, a computer program for

557   maximum-entropy method (MEM) analysis and its performance in the MEM-based pattern fitting.

558   Powder Diffraction, 28, 184-193.

17

559   Morgan, V. and Erd, R.C. (1969) Minerals of the Kramer borate district, California. California

560 Division of Mines and Geology Mineral Information Service, 22, pp. 143-153 and 165-172.

561   Noble, L.F. (1926) Borate deposits in the Kramer district, Kern County, California. U.S.

562 Geological Survey Bulletin, 785, 45-61.

563   Obert, L. and Long, A.E. (1962) Underground borate mining, Kern County, California. U.S.

564 Bureau of Mines Report of Investigation, 6110, 1-12.

565   Palmer M.R. and Swihart, G.H. (1996) Boron Isotope Geochemistry: An Overview. In L.M.

566 Anovitz, E.S. Grew (Eds.), Boron: Mineralogy, Petrology, and Geochemistry, Review in Mineralogy

567 33, Mineralogical Society of America, Chantilly, pp. 709-744.

568   Puffer, J.H. (1975) The Kramer borate mineral assemblage. Mineralogical Record, 6, 84-91.

569   Rauch, H., and Waschkowski, W. (2002) Neutron Scattering Lengths. In A.J. Dianoux, G.

570 Lander (Eds.), Neutron Data Booklet, first ed., Institut Laue Langevin, Grenoble, pp. 1-18.

571   Schaller, W. T. (1927) Kernite, a new sodium borate. American Mineralogist, 12, 24-25.

572   Schaller, W. T. (1930) Borate minerals from the Kramer district, Mohave Desert, California.

573 U.S. Geological Survey Professional Paper, 158, 137-170.

574   Sears, V.F. (1986) Neutron Scattering Lengths and Cross-Sections. In K. Sköld and D.L.

575 Price, Eds., Neutron Scattering, Methods of Experimental Physics, Vol. 23A, Academic Press, New

576 York, pp. 521-550.

577   Sennova, N.A., Bubnova, R.S., Filatov, S.K., Paufler, P., Meyer, D.C., Levin, A.A., and

578 Polyakova, I.G. (2005) Room, low, and high temperature dehydration and phase transition of kernite

579 in vacuum and in air. Crystal Research and Technology, 40, 563–572.

580   Sheldrick, G.M. (1997) SHELXL-97. Programs for crystal structure determination and

581 refinement. University of Göttingen, Germany.

582   Sheldrick, G.M. (2008) A short history of SHELX. Acta Crystallographica, A64, 112-122.

583   Siefke, J.W. (1991) The Boron open Pit Mine at the Kramer Borate Deposit. The Diversity of

584 Mineral and Energy Resources of Southern California. In M.A. McKibben, Ed., Society of Economic

585 Geologist Guidebook Series, 12, 4-15.

586   Silva, M., O'Bannon, E.F., and Williams, Q. (2018) A vibrational spectroscopic study of

587 kernite to 25 GPa: Implications for the high-pressure stability of borate polyhedra. American

588 Mineralogist, 103, 1306–1318.

589   Steiner, T. (1998) Opening and narrowing of the water H-O-H angle by hydrogen-bonding

590 effects: Re-inspection of neutron diffraction data. Acta Crystallographica, B54, 464-470.

18

591   U.S.G.S. (2018) Mineral commodity summaries 2018. U.S. Geological Survey, 200 p., Reston,

592 Virginia, U.S.A.

593   U.S.G.S. (2019) Mineral commodity summaries 2019. U.S. Geological Survey, 200 p., Reston,

594 Virginia, U.S.A.

595   Yen, F. and Gao, T. (2015) Dielectric Anomaly in Ice near 20 K: Evidence of Macroscopic

596   Quantum Phenomena. Journal of Physical Chemistry Letter, 6, 2822−2825.

597

598

599

600

601

602

603

19

604 Table 1. REE concentration by ICP-AES (see text for details).

605

	%m/m	ICP-AES (nm)	LOD	LOQ
Ce_2O_3	< LOD	413.764	0.003	0.01
Dy_2O_3	< LOD	353.170	0.0001	0.0003
Er_2O_3	< LOD	369.265	0.002	0.007
Eu_2O_3	< LOD	381.967	0.0001	0.0003
Gd_2O_3	< LOD	342.247	0.0003	0.001
Ho_2O_3	< LOD	345.600	0.0001	0.0003
La_2O_3	< LOD	398.852	0.0001	0.0003
Lu_2O_3	< LOD	261.542	0.0002	0.0006
Nd_2O_3	< LOD	406.109	0.0002	0.0006
Pr_2O_3	< LOD	390.844	0.0002	0.0006
Sm_2O_3	< LOD	359.260	0.0005	0.002
Sc_2O_3	< LOD	361.383	0.0005	0.002
Tb_2O_3	< LOD	350.917	0.0005	0.002
Tm_2O_3	< LOD	313.126	0.004	0.015
Yb_2O_3	< LOD	328.937	0.0001	0.0003
Y_2O_3	< LOD	371.029	0.0001	0.0003
ThO_2	< LOD	283.730	0.001	0.004
UO_2	< LOD	385.958	0.01	0.04

Note: LOD: Limit of detection (3σ); LOQ: Limit of quantification (10σ)

616

617 Table 2. Concentration of other minor elements by ICP-AES (see text for details).

618

	%m/m	ICP-AES (nm)		%m/m	ICP-AES (nm)
Li_2O	< 0.01	670.784	NiO	< 0.01	231.604
MgO	0.01	285.213	CuO	< 0.01	327.393
K_2O	0.02	766.490	Ag_2O	< 0.01	328.068
Rb_2O	< 0.02	780.023	ZnO	< 0.01	206.200
Cs_2O	< 0.02	455.531	CdO	< 0.01	228.802
BeO	< 0.01	313.107	Al_2O_3	0.01	396.153
CaO	< 0.01	317.933	Tl_2O	< 0.02	190.801
BaO	< 0.02	233.527	PbO	< 0.05	220.353
TiO_2	< 0.01	334.940	P_2O_5	< 0.02	213.617
ZrO_2	< 0.01	343.823	As_2O_3	< 0.02	193.696
V_2O_5	< 0.02	292.464	Sb_2O_3	< 0.02	206.836
Cr_2O_3	< 0.01	267.716	Bi_2O_3	< 0.02	223.061
MoO_3	< 0.02	202.031	SiO_2	0.01	251.611
MnO	< 0.01	257.610	SrO	< 0.01	407.771
Fe_2O_3	< 0.01	238.204	B_2O_3	*	249.677
CoO	< 0.01	228.616	Na_2O	*	589.592

* data were not reproducible and therefore discarded

627   Table 3. Representative chemical composition of kernite from Kramer Deposit (Kern County,
628   California), and empirical formula recalculated on the basis of eleven anions.
629
630
631
632
633
634
635
636
637
638
639
640
641
642
643
644
645
646
647
648
649
650
651
652
653
654
655
656
657
658
659
660
661
662
663
664
665
666
667
668
669
670
671
672
673
674
675
676
677
678

Oxides	Wt%	e.s.d.
B_2O_3	50.90	± 0.20
Na_2O	22.55	± 0.20
SiO_2	0.01	± n.d
Al_2O_3	0.01	± n.d
MgO	0.01	± n.d
K_2O	0.02	± n.d
F^-	0.01	± n.d
H_2O	26.40	± 0.20
TOTAL	99.91	

Elements	a.p.f.u.
B^{3+}	3.99
Na^+	1.99
Si^{4+}	<0.01
Al^{3+}	<0.01
Mg^{2+}	<0.01
K^+	<0.01
F^-	<0.01
H^+	8.02

Empirical formula:
$Na_{1.99}B_{3.99}O_6(OH)_2 \cdot 3.01 H_2O$
Ideal formula:
$Na_2B_4O_6(OH)_2 \cdot 3H_2O$

21

679

680   Table 4 (*deposited*). Details of neutron and X-ray data collections and refinements of kernite.

681

682

683

T (K)	20	293
Crystal shape	Prism	Prism
Crystal volume (mm)	3 x 2 x 2	0.22 x 0.12 x 0.11
Crystal colour	White	White
Unit-cell parameters	$a = 6.996(1)$ Å	$a = 6.9983(3)$ Å
	$b = 9.128(3)$ Å	$b = 9.1375(3)$ Å
	$c = 15.608(3)$ Å	$c = 15.6389(7)$ Å
	$\beta = 109.06(3)°$	$\beta = 108.832(5)°$
	$V = 942.0(4)$ Å^3	$V = 946.53(7)$ Å^3
Chemical formula	$Na_2B_4O_6(OH)_2 \cdot 3H_2O$	$Na_2B_4O_6(OH)_2 \cdot 3H_2O$
Space Group	$P\,2_1/c$	$P\,2_1/c$
Z	4	4
Radiation type, λ (Å)	Neutron CW, 0.8347	X-ray, Mo$K\alpha$
Diffractometer	D9 four-circle - ILL	Rigaku XtaLABSynergy-i
Data-collection method	ω-scans, ω-2θ scans	ω-scans
$d_{min.}$ (Å)	0.59	0.71
	$-10 \le h \le +10$	$-9 \le h \le +8$
	$0 \le k \le +18$	$-12 \le k \le +12$
	$-23 \le l \le +24$	$-19 \le l \le +20$
Measured reflections	3434	13010
Unique reflections	3161	2296
Unique reflections with $F_o > 4\sigma(F_o)$	2656	1908
Refined parameters	226	193
Extinction coeff.	0.014(2)	0.001(1)
R_{Int}	0.0488	0.0361
R_σ	0.0557	0.0259
R_1 (F) with $F_o > 4\sigma(F_o)$	0.0723	0.0324
R_1 (F) for all reflections	0.0884	0.0412
$wR_2(F^2)$	0.1491	0.0655
GooF	1.636	1.519
Residuals (fm/Å^3, e^-/Å^3)	-1.9/+2.5	-0.3/+0.5

Note: Statistical parameters according to the Shelxl-97 definition (Sheldrick 1997, 2008).

684
685
686
687
688
689
690
691
692
693
694
695
696
697
698
699
700
701
702
703

22

704 Table 5 (_deposited_). Refined fractional atomic coordinates and equivalent/isotropic displacement
705 factors (Å^2) of kernite, based on the X-ray structure refinement at 293 K and neutron refinement at
706 20 K. U_{eq} is defined as one third of the trace of the orthogonalised U_{ij} tensor.
707
708

Site	s.o.f.	x/a	y/b	z/c	U_{eq}	s.o.f.	x/a	y/b	z/c	U_{eq}/U_{iso}
		X-ray	*293 K*				*Neutron*	*20 K*		
Na1	1	0.31944(12)	0.46480(8)	0.31093(6)	0.0245(2)	1	0.3190(4)	0.4638(2)	0.3102(2)	0.0067(7)
Na2	1	0.18563(14)	0.36644(9)	0.07250(6)	0.0353(2)	1	0.1869(4)	0.3681(2)	0.0703(2)	0.0073(8)
O1	1	0.4874(2)	0.52527(13)	0.10281(8)	0.0182(3)	1	0.4865(2)	0.52517(13)	0.10184(13)	0.0050(4)
O2	1	0.55971(19)	0.59894(13)	0.25905(8)	0.0157(3)	1	0.5610(2)	0.59800(12)	0.25950(12)	0.0038(4)
O3	1	0.23252(19)	0.70586(14)	0.23145(9)	0.0192(3)	1	0.2321(2)	0.70429(13)	0.23132(13)	0.0046(4)
O4	1	0.46514(18)	0.35087(12)	0.20889(8)	0.0138(3)	1	0.4642(2)	0.34976(12)	0.20771(12)	0.0038(4)
O5	1	0.79157(19)	0.44857(14)	0.21541(9)	0.0200(3)	1	0.7920(2)	0.44738(13)	0.21481(13)	0.0046(4)
O6	1	0.0623(2)	0.29066(16)	0.24061(11)	0.0293(4)	1	0.0648(2)	0.28819(15)	0.24073(14)	0.0062(4)
O7	1	0.4154(2)	0.70621(16)	-0.00985(10)	0.0301(4)	1	0.4169(3)	0.70779(14)	-0.01111(14)	0.0074(5)
O8	1	0.2249(3)	0.53337(18)	0.43187(11)	0.0338(4)	1	0.2223(3)	0.53220(17)	0.43146(15)	0.0105(5)
O9	1	0.5654(2)	0.27258(13)	0.36300(9)	0.0188(3)	1	0.5643(2)	0.27324(13)	0.36308(13)	0.0050(4)
O10	1	-0.0389(2)	0.56220(18)	0.08468(11)	0.0311(4)	1	-0.0380(3)	0.55883(16)	0.08588(15)	0.0080(5)
O11	1	0.1674(2)	0.11763(17)	0.07646(11)	0.0294(4)	1	0.1662(3)	0.11800(15)	0.07555(14)	0.0074(5)
B1	1	0.4469(3)	0.6680(2)	0.07836(14)	0.0173(4)	1	0.4480(2)	0.66898(13)	0.07755(14)	0.00330(18)
B2	1	0.5532(3)	0.2325(2)	0.26885(13)	0.0137(4)	1	0.5530(2)	0.23179(13)	0.26849(13)	0.00260(18)
B3	1	0.5736(3)	0.4804(2)	0.19976(14)	0.0141(4)	1	0.5738(2)	0.48006(13)	0.19901(13)	0.00272(17)
B4	1	0.1323(3)	0.8137(2)	0.25825(15)	0.0184(4)	1	0.1300(2)	0.81241(13)	0.25821(13)	0.00304(18)
H1	1	0.264(4)	0.100(4)	0.1327(16)	0.072(10)	1	0.2679(5)	0.1025(4)	0.1359(3)	0.0207(10)
H2	1	0.106(4)	0.1942(16)	0.2510(19)	0.056(9)	1	0.1110(6)	0.1887(4)	0.2510(3)	0.0202(8)
H3	1	0.048(4)	0.622(3)	0.1249(19)	0.067(10)	1	0.0591(5)	0.6211(4)	0.1296(3)	0.0195(9)
H4	1	0.431(5)	0.626(2)	-0.0447(19)	0.072(10)	1	0.4388(6)	0.6245(4)	-0.0462(3)	0.0195(9)
H5	1	-0.109(4)	0.523(3)	0.120(2)	0.071(10)	1	-0.1151(7)	0.5161(5)	0.1215(3)	0.0247(10)
H6	1	0.293(5)	0.620(3)	0.454(2)	0.088(12)	1	0.2962(6)	0.6219(4)	0.4549(3)	0.0214(8)
H71	0.40(3)	0.197(10)	0.058(6)	0.033(4)	0.046(8)	0.361(14)	0.2060(18)	0.0590(12)	0.0305(11)	0.023(3)
H72	0.60(3)	0.252(7)	0.478(4)	0.485(2)	0.046(8)	0.639(14)	0.2305(10)	0.4714(6)	0.4858(6)	0.0192(17)
H81	0.60(3)	0.048(5)	0.082(5)	0.081(3)	0.046(8)	0.639(14)	0.0370(9)	0.0838(7)	0.0774(5)	0.0208(14)
H82	0.40(3)	0.092(5)	0.568(7)	0.418(5)	0.046(8)	0.361(14)	0.0729(19)	0.5631(12)	0.4193(9)	0.024(2)

709
710
711
712
713
714
715

23

716

717 Table 6 (*deposited*). Refined displacement parameters (Å^2) of kernite in the expression: -
718 $2\pi^2[(ha^*)^2 U_{11} + \ldots + 2hka^*b^* U_{12} + \ldots + 2klb^*c^* U_{23}]$, based on the X-ray refinement at 293 and neutron
719 structure refinement at 20 K.

720

721

$T = 293\ K$	U_{11}	U_{22}	U_{33}	U_{23}	U_{13}	U_{12}
Na1	0.0299(5)	0.0193(4)	0.0302(5)	0.0008(3)	0.0177(4)	0.0011(3)
Na2	0.0352(5)	0.0245(5)	0.0360(5)	0.0007(4)	-0.0027(4)	-0.0016(4)
O1	0.0291(7)	0.0128(6)	0.0134(6)	0.0002(5)	0.0078(5)	0.0018(5)
O2	0.0222(7)	0.0105(6)	0.0136(6)	-0.0005(5)	0.0048(5)	0.0020(5)
O3	0.0171(7)	0.0162(6)	0.0249(7)	-0.0048(5)	0.0078(5)	-0.0035(5)
O4	0.0146(6)	0.0103(6)	0.0165(6)	0.0013(5)	0.0052(5)	0.0007(4)
O5	0.0174(6)	0.0165(6)	0.0288(7)	0.0020(5)	0.0112(5)	-0.0001(5)
O6	0.0191(7)	0.0249(8)	0.0462(9)	0.0009(6)	0.0138(6)	0.0025(6)
O7	0.0527(8)	0.0212(7)	0.0172(6)	0.0021(5)	0.0126(6)	0.0074(6)
O8	0.0398(8)	0.0335(8)	0.0306(7)	-0.0049(6)	0.0150(6)	-0.0050(6)
O9	0.0286(7)	0.0131(6)	0.0148(6)	-0.0013(5)	0.0073(5)	-0.0028(5)
O10	0.0331(8)	0.0358(8)	0.0249(8)	-0.0046(7)	0.0103(7)	-0.0087(7)
O11	0.0310(7)	0.0292(7)	0.0248(7)	-0.0015(6)	0.0048(6)	-0.0006(6)
B1	0.0216(11)	0.0154(10)	0.0152(10)	0.0008(8)	0.0064(8)	0.0006(8)
B2	0.0167(10)	0.0112(9)	0.0133(10)	0.0007(7)	0.0051(8)	0.0002(7)
B3	0.0177(10)	0.0113(9)	0.0148(10)	0.0002(7)	0.0073(8)	0.0005(7)
B4	0.0181(10)	0.0190(10)	0.0191(10)	0.0016(8)	0.0071(8)	-0.0004(8)

Note: All the H sites were modelled isotropically in the X-ray structure refinement at 293 K

722
723
724
725
726
727
728
729
730
731
732
733
734
735
736
737
738
739
740
741
742
743
744

24

745
746
747
748

$T = 20\ K$	U_{11}	U_{22}	U_{33}	U_{23}	U_{13}	U_{12}
Na1	0.0050(9)	0.0059(6)	0.0090(15)	0.0005(7)	0.0019(10)	0.0004(6)
Na2	0.0055(9)	0.0066(6)	0.0084(15)	0.0009(7)	0.0005(10)	-0.0010(6)
O1	0.0054(5)	0.0035(3)	0.0052(8)	-0.0004(4)	0.0003(6)	0.0009(4)
O2	0.0026(5)	0.0038(3)	0.0049(7)	-0.0002(4)	0.0013(5)	0.0005(3)
O3	0.0019(4)	0.0047(3)	0.0069(7)	-0.0010(4)	0.0012(5)	-0.0006(3)
O4	0.0016(5)	0.0037(3)	0.0055(7)	0.0008(3)	0.0002(5)	-0.0003(3)
O5	0.0023(4)	0.0049(3)	0.0065(7)	0.0005(4)	0.0014(5)	0.0005(3)
O6	0.0028(5)	0.0069(4)	0.0094(7)	0.0000(4)	0.0026(5)	0.0011(4)
O7	0.0098(6)	0.0056(4)	0.0065(9)	0.0006(4)	0.0021(6)	0.0017(4)
O8	0.0084(7)	0.0106(5)	0.0123(11)	-0.0035(6)	0.0030(7)	-0.0029(5)
O9	0.0040(5)	0.0044(3)	0.0062(9)	-0.0007(4)	0.0011(6)	-0.0007(4)
O10	0.0053(6)	0.0083(4)	0.0093(10)	-0.0009(5)	0.0008(7)	-0.0006(4)
O11	0.0043(6)	0.0075(4)	0.0094(10)	0.0000(5)	0.0009(6)	-0.0002(4)
H1	0.0159(14)	0.0222(12)	0.020(2)	0.0008(12)	0.0010(13)	-0.0002(11)
H2	0.0178(12)	0.0159(9)	0.0264(16)	0.0027(10)	0.0063(11)	0.0062(9)
H3	0.0150(12)	0.0202(11)	0.0232(18)	-0.0044(11)	0.0059(12)	-0.0085(10)
H4	0.0224(15)	0.0163(10)	0.020(2)	-0.0008(11)	0.0068(14)	-0.0002(11)
H5	0.0213(16)	0.0244(14)	0.029(2)	0.0010(15)	0.0095(16)	-0.0038(14)
H6	0.0214(13)	0.0185(10)	0.0235(16)	-0.0045(11)	0.0064(11)	-0.0083(10)
H71	0.018(4)	0.022(3)	0.029(7)	-0.005(4)	0.008(4)	0.000(3)
H72	0.021(2)	0.0195(17)	0.016(3)	0.0053(18)	0.005(2)	0.0008(17)
H81	0.0170(19)	0.0234(16)	0.022(2)	-0.0018(15)	0.0058(14)	-0.0013(13)
H82	0.023(3)	0.024(2)	0.024(3)	0.0001(10)	0.0078(11)	-0.0002(10)

Note: B1, B2, B3, and B4 sites were modelled isotropically in the neutron structure refinement at 20 K

749
750

25

751 Table 7. Relevant bond distances (Å) and angles (°) based on the X-ray refinement at 293 K and
752 neutron structure refinement at 20 K.

X-ray *T = 293 K*					
Na1-O8	2.2835(18)	O11-H1	0.94(2)	O8-H72	0.93(4)
Na1-O6	2.3879(17)	O11-H1*	0.97	O8-H72*	0.96
Na1-O4	2.3918(14)	O11···O2	2.669(2)	O8···O11	2.787(3)
Na1-O9	2.4095(15)	H1···O2	1.74(2)	H72···O11	1.93(4)
Na1-O2	2.4226(14)	O11-H1···O2	170(2)	O8-H72···O11	152(3)
Na1-O3	2.5058(15)				
		O11-H71	0.94(7)	O8-H82	0.94(4)
Na2-O11	2.2790(17)	O11-H71*	0.97	O8-H82*	0.97
Na2-O4	2.3880(15)	O11···O8	2.787(3)	O8···O11	2.814(3)
Na2-O10	2.4274(18)	H71···O8	1.86(6)	H82···O11	1.90(5)
Na2-O10'	2.4287(19)	O11-H71···O8	169(5)	O8-H82···O11	163(4)
Na2-O1	2.4791(16)				
Na2-O6	3.099(4)	O11-H81	0.92(4)	H6-O8-H72	102(3)
		O11-H81*	0.95	H6-O8-H82	100(4)
B1-O1	1.363(2)	O11···O8	2.814(3)		
B1-O7	1.370(2)	H81···O8	1.91(4)		
B1-O9	1.346(2)	O11-H81···O8	168(3)		
B2-O2	1.443(2)	H1-O11-H71	108(5)		
B2-O4	1.434(2)	H1-O11-H81	106(3)		
B2-O9	1.493(2)				
B2-O3	1.520(2)	O6-H2	0.93(2)		
		O6-H2*	0.96		
B3-O1	1.497(2)	O6···O5	3.292(2)		
B3-O2	1.450(2)	H2···O5	2.36(2)		
B3-O4	1.438(2)	O6-H2···O5	177(1)		
B3-O5	1.493(2)				
		O10-H3	0.91(3)		
B4-O3	1.352(2)	O10-H3*	0.94		
B4-O5	1.353(2)	O10···O3	2.790(2)		
B4-O6	1.384(3)	H3···O3	1.91(3)		
		O10-H3···O3	164(3)		
O1-B1-O9	122.8(2)	O7-H4	0.94(3)		
O7-B1-O9	118.7(2)	O7-H4*	0.97		
O1-B1-O7	118.5(2)	O7···O1	2.773(2)		
		H4···O1	1.84(3)		
O4-B2-O2	111.24(14)	O7-H4···O1	169(2)		
O4-B2-O9	109.61(14)				
O2-B2-O9	110.91(14)	O10-H5	0.92(4)		
O4-B2-O3	109.58(14)	O10-H5*	0.95		
O2-B2-O3	107.95(14)	O10···O5	2.869(2)		
O9-B2-O3	107.46(14)	H5···O5	1.96(4)		
		O10-H5···O5	168(3)		
O4-B3-O2	113.89(15)				
O4-B3-O5	111.57(14)	H3-O10-H5	101(3)		
O2-B3-O5	108.45(15)				
O4-B3-O1	105.85(14)	O8-H6	0.93(3)		
O2-B3-O1	110.79(14)	O8-H6*	0.96		
O5-B3-O1	106.00(14)	O8···O7	2.736(2)		
		H6···O7	1.81(3)		
O3-B4-O5	124.41(17)	O8-H6···O7	176(3)		
O3-B4-O6	120.31(17)				
O5-B4-O6	115.28(17)				

* Bond distance corrected for "riding motion" effect, following Busing and Levy (1964)

26

795
796
797
798

Neutron *T = 20 K*					
Na1-O8	2.294(5)	O11-H1	0.988(4)	O8-H72	1.000(8)
Na1-O6	2.377(2)	O11-H1*	1.003	O8-H72*	1.014
Na1-O4	2.395(4)	O11···O2	2.663(3)	O8···O11	2.769(3)
Na1-O9	2.393(2)	H1···O2	1.68084)	H72···O11	1.800(9)
Na1-O2	2.422(4)	O11-H1···O2	173.0(4)	O8-H72···O11	162.2(7)
Na1-O3	2.493(3)				
		O11-H71	0.995(17)	O8-H82	1.038(13)
Na2-O11	2.291(3)	O11-H71*	1.012	O8-H82*	1.051
Na2-O4	2.382(3)	O11···O8	2.769(3)	O8···O11	2.796(3)
Na2-O10	2.411(3)	H71···O8	1.792(17)	H82···O11	1.773(14)
Na2-O10'	2.411(4)	O11-H71···O8	167(1)	O8-H82···O11	168(1)
Na2-O1	2.453(3)				
Na2-O6	3.134(21)	O11-H81	0.966(7)	H6-O8-H72	105.8(5)
		O11-H81*	0.981	H6-O8-H82	102.7(7)
B1-O1	1.3685(17)	O11···O8	2.796(3)		
B1-O7	1.375(3)	H81···O8	1.835(7)		
B1-O9	1.350(3)	O11-H81···O8	173.1(6)		
B2-O2	1.4457(16)	H1-O11-H71	108.4(7)		
B2-O4	1.4353(18)	H1-O11-H81	108.3(5)		
B2-O9	1.501(3)				
B2-O3	1.523(3)	O6-H2	0.960(4)		
		O6-H2*	0.978		
B3-O1	1.496(3)	O6···O5	3.273(2)		
B3-O2	1.454(3)	H2···O5	2.316(4)		
B3-O4	1.445(2)	O6-H2···O5	174.9(3)		
B3-O5	1.494(3)				
		O10-H3	0.974(4)		
B4-O3	1.363(3)	O10-H3*	0.988		
B4-O5	1.3577(17)	O10···O3	2.772(2)		
B4-O6	1.385(3)	H3···O3	1.818(4)		
		O10-H3···O3	165.7(4)		
O1-B1-O9	122.5(2)	O7-H4	0.977(4)		
O7-B1-O9	118.97(13)	O7-H4*	0.990		
O1-B1-O7	118.56(18)	O7···O1	2.759(3)		
		H4···O1	1.787(4)		
O4-B2-O2	110.93(11)	O7-H4···O1	172.4(3)		
O4-B2-O9	109.47(14)				
O2-B2-O9	110.90(18)	O10-H5	0.974(6)		
O4-B2-O3	109.79(18)	O10-H5*	0.994		
O2-B2-O3	107.92(13)	O10···O5	2.840(3)		
O9-B2-O3	107.76(12)	H5···O5	1.885(6)		
		O10-H5···O5	165.8(5)		
O4-B3-O2	113.7(2)				
O4-B3-O5	111.38(11)	H3-O10-H5	102.9(5)		
O2-B3-O5	108.49(11)				
O4-B3-O1	105.57(11)	O8-H6	0.974(4)		
O2-B3-O1	111.29(11)	O8-H6*	0.988		
O5-B3-O1	106.2(2)	O8···O7	2.737(2)		
		H6···O7	1.766(4)		
O3-B4-O5	123.67(19)	O8-H6···O7	175.0(4)		
O3-B4-O6	116.01(17)				
O5-B4-O6	120.32(12)				

* Bond distance corrected for "riding motion" effect, following Busing and Levy (1964)

799
800
801
802
803
804
805
806
807
808
809
810
811
812
813
814
815
816
817
818
819
820
821
822
823
824
825
826
827
828
829
830
831
832
833
834
835
836
837
838
839

27

840   Figure 1. The crystal structure of kernite viewed down [010] (*left side*), along with the infinite chains
841   of 3-fold rings (3B:Δ + 2T units) running along [010] (*right side*), based on the neutron structure
842   refinement of this study (intensity data collected at 20 K). Displacement ellipsoid probability factor:
843   70%.
844
845
846
847
848
849
850
851
852
853
854
855
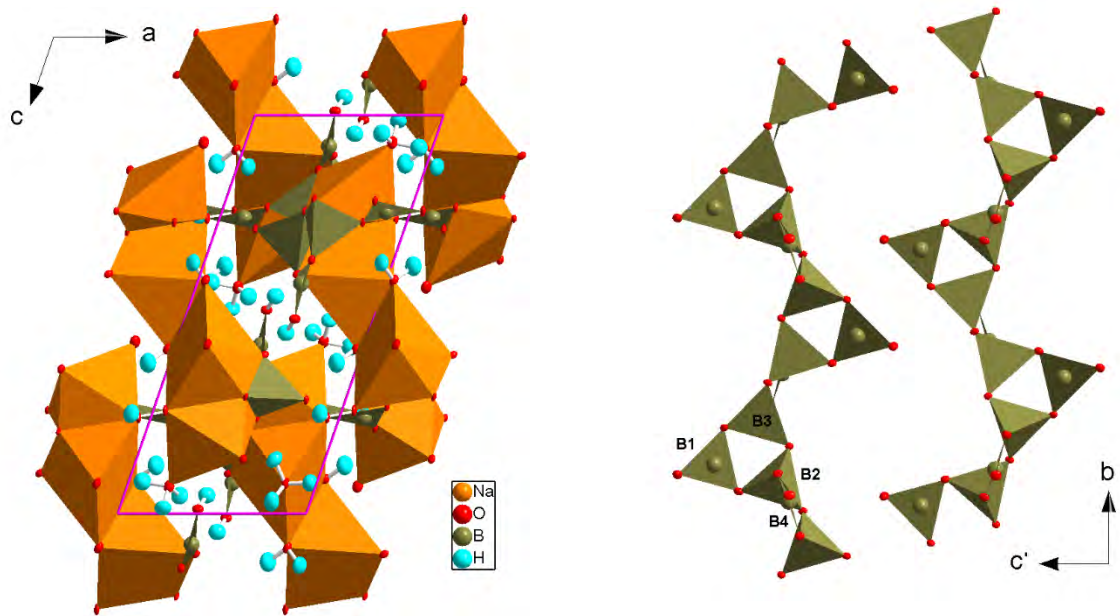
856 Figure 2. Positional disorder of the H sites in the structure of kernite, based on the neutron structure
857 refinement of this study (intensity data collected at 20 K). The mutually exclusive configurations are:
858 (H6-O8-H82 + H1-O11-H71) and (H6-O8-H72 + H1-O11-H81); *s.o.f.*(H2) = 1, *s.o.f.*(H1) = 1,
859 [*s.o.f.*(H72)+*s.o.f.*(H82)] = 1, [*s.o.f.*(H71)+*s.o.f.*(H81)] = 1. Displacement ellipsoid probability factor:
860 70%.

29
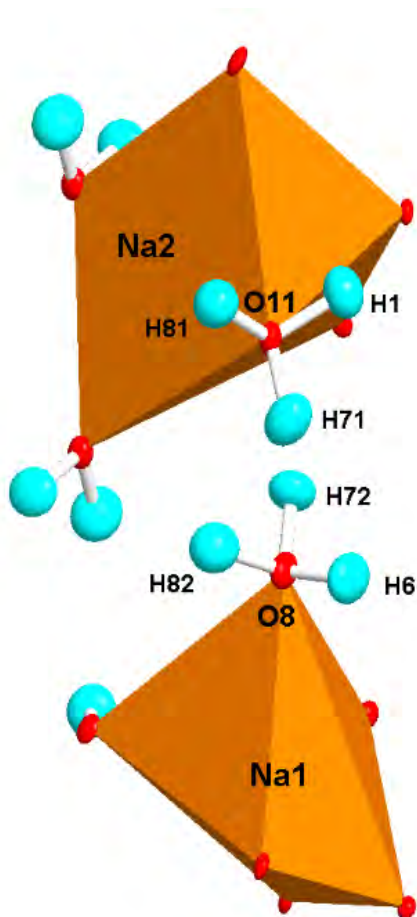
910 Figure 3. Section of the nuclear density function, corresponding to the (0.1, 0.5, 0.6) plane (which
911 contains O8, O11 and symmetry-related H_2O molecules), calculated using the maximum-entropy
912 method applied to the neutron intensity data collected at 20 K. A grid of 256 x 256 x 256 voxels was
913 used to obtain a detailed density map. Further details are given in the text. Graphical representation
914 by VESTA. Colour bar: maxima at the top, minima at the bottom of the nuclear density. Atom labels
915 showing a prime involve that those atoms are generated by application of a symmetry operator.
916
917
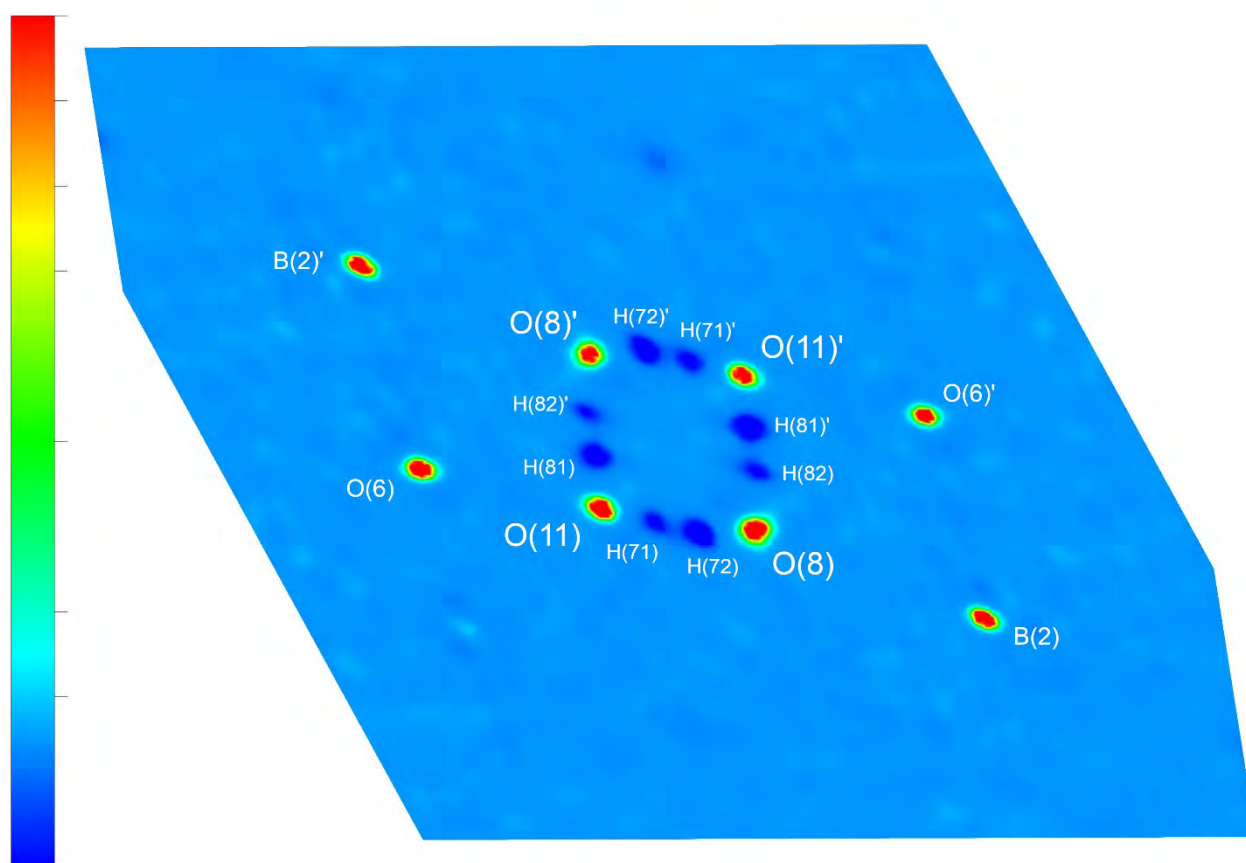
918
919
920
921
922
923
924
925
926
927
928

929
930
931   Figure 4. The complex H-bonding network into the crystal structure of kernite, based on the neutron
932   structure refinement (data collected at 20 K). Details in Table 7. Displacement ellipsoid probability
933   factor: 70%.
934
935
936
937
938
939
940
941
942
943
944
945
946
947

31